



1 **The Different Dynamic Influences of Typhoon Kalmaegi** 2 **on two Pre-existing Anticyclonic Ocean Eddy**

3 Yihao He¹, Xiayan Lin^{1,2,*}, Guoqing Han¹, Yu Liu^{1,3} and Han Zhang^{2,3,*}

4 ¹ Marine Science and Technology College, Zhejiang Ocean University, Zhoushan 316022, China;

5 ² State Key Laboratory of Satellite Ocean Environment Dynamics, Second Institute of Oceanography,
6 Ministry of Natural Resources, Hangzhou 310012, China;

7 ³ Southern Marine Science and Engineering Guangdong Laboratory (Zhuhai), Zhuhai 519082, China

8 **Correspondence*: Xiayan Lin (linxiayan@zjou.edu.cn) and Han Zhang (zhanghan@sio.org.cn)

9

10 **Abstract:** Using multi-source observational data and GLORYS12V1 reanalysis data, we conducted a
11 comparative analysis of different responses of two warm eddies, AE1 and AE2 in the northern South
12 China Sea to Typhoon Kalmaegi during September 2014. The findings of our research are as follows: (1)
13 For horizontal distribution, the area and the sea surface temperature (SST) of AE1 and AE2 decreased
14 by about 31% (36%) and 0.4 °C (0.6 °C). The amplitude, Rossby number (R_o) and eddy kinetic energy
15 (EKE) of AE1 increased by 1.3 cm, 1.4×10^{-2} and $107.2 \text{ cm}^2 \text{ s}^{-2}$ after the typhoon, respectively, while
16 AE2 weakened and the amplitude, vorticity and EKE decreased by 3.1 cm, 1.6×10^{-2} and $38.5 \text{ cm}^2 \text{ s}^{-2}$,
17 respectively. (2) In vertical direction, AE1 demonstrated enhanced convergence, leading to an increase
18 in temperature and a decrease in salinity above 150 m. The response below the mixing layer depth (MLD)
19 was particularly prominent (1.3 °C). In contrast, AE2 experienced cooling and a decrease in salinity
20 above the MLD. Below the MLD, it exhibited a subsurface temperature drop and salinity increase due to
21 the upwelling of cold water induced by the suction effect of the typhoon. (3) The disparity in the
22 responses of the two warm eddies can be attributed to their different positions relative to Typhoon
23 Kalmaegi. Warm eddy AE1, with its center located on the left side of the typhoon's path, experienced a
24 positive work effect as the typhoon passed by. This induced a strong negative wind stress curl and
25 triggered a negative Ekman pumping velocity (EPV), further enhanced by the converging sinking of the
26 upper warm water, thereby strengthening AE1. On the other hand, warm eddy AE2, situated closer to
27 the center of the typhoon, weakened due to the cold suction caused by the strong positive wind stress
28 curl in the typhoon's center. These findings underscore the importance of relative positions of eddies in
29 their interactions with typhoons.



30 **1. Introduction**

31 Typhoons, as they traverse the vast ocean, interact with oceanic mesoscale processes, particularly
32 with mesoscale eddies, representing a crucial aspect of air-sea interaction (Shay and Jaimes, 2010; Lu et
33 al., 2016; Song et al., 2018; Ning et al., 2019; Sun et al., 2023). The South China Sea (SCS) experiences
34 an average of six typhoons passing through each year (Wang et al., 2007). Meanwhile, the northern part
35 of the South China Sea (NSCS) encounters frequent eddy activities due to the influence of the Asian
36 monsoon, intrusion of the Kuroshio Current, and the impact of topography (Xiu et al., 2010; Chen et al.,
37 2011). This unique setting offers an exceptional opportunity to investigate the generation, evolution, and
38 termination of mesoscale eddies and their interaction with typhoons.

39 On one hand, tropical cyclones (TCs) derive their development and sustenance energy from the ocean.
40 Pre-existing mesoscale eddies play a crucial role in the feedback mechanism between the ocean and TCs.
41 Cyclonic eddies (cold eddies) enhance the sea surface cooling effect under TC conditions, resulting in
42 TCs weakening, due to their thermodynamic structure and cold-water entrainment processes that reduce
43 the heat transfer from the sea surface to the typhoon through air-sea interaction (Ma et al., 2017; Yu et
44 al., 2021). In contrast, anticyclonic eddies (warm eddies) suppress this cooling effect, leading to TC
45 intensification (Shay et al., 2000; Walker et al., 2005; Lin et al., 2011; Wang et al., 2018). Warm eddies
46 have a thicker upper mixed layer, which stores more heat. When a typhoon passes through a warm eddy,
47 it increases sensible heat and water vapor in the typhoon's center, which are closely related to the
48 typhoon's intensification (Wada and Usui, 2010; Huang et al., 2022). Furthermore, the downwelling
49 within warm eddies hinders the upwelling of cold water, reducing the apparent sea surface cooling caused
50 by the typhoon. This weakens the oceanic negative feedback effect and helps to sustain or even strengthen
51 the typhoon's development.

52 On the other hand, TCs can induce various oceanic processes such as local advection, vertical mixing,
53 and upwelling, leading to a decrease in sea surface temperature (SST). The cooling effect typically ranges
54 from 2-4°C and can reach up to 10°C under extreme conditions (Price, 1981; Wu et al., 2011; Han et al.,
55 2012). The distribution of typhoon wind stress and variations in vertical mixing cause different cooling
56 patterns on both sides of the typhoon track in the upper ocean. Generally, the right side exhibits stronger
57 cooling of the SST in the northern hemisphere (Stramma et al., 1986; Vincent et al., 2012; Mei et al.,
58 2015; Mitarai and McWilliams, 2016). TCs also have a notable impact on the intensity, size, and



59 movement of mesoscale eddies. In general, TCs strengthen cold eddies and can even lead to the formation
60 of new cyclonic eddies in certain situations (Sun et al., 2014), while TCs accelerate the dissipation of
61 anticyclonic eddies (Zhang et al., 2020). The interaction between TCs and eddies directly affects the
62 local upper ocean structure and circulation system.

63 The strengthening effect of TCs on cold eddies is related to the positions between cold eddies and
64 TCs, the intensity of eddies, and TC-induced geostrophic response (Lu et al., 2016; Yu et al., 2019; Lu
65 et al., 2023). Cyclonic eddies on the left side of the typhoon track were more intensely affected by the
66 typhoon than eddies on the right side, and eddies with shorter lifespans or smaller radii are more
67 susceptible to the influence of typhoons. The dynamic adjustment process of eddy and the upwelling
68 induced by the typhoon itself leads to changes in the three-dimensional structure of the cyclonic eddies,
69 including ellipse deformation and re-axisymmetrization on the horizontal plane, resulting in eddy
70 intensification. The presence of cold eddies not only exacerbates the sea surface cooling in the post-
71 typhoon cold eddy region but also accompanies a decrease in sea level anomaly (SLA), deepening of the
72 mixed layer, a strong cooling in the subsurface, increased chlorophyll-a concentration within the eddy,
73 and substantial increases in eddy kinetic energy (EKE) and available potential energy (Shang et al., 2015;
74 Liu and Tang, 2018; Li et al., 2021; Ma et al., 2021).

75 Generally, typhoons lead to a reduction of warm eddies, while the sea surface cooling is not
76 significant, typically within 1°C. However, there is a noticeable cooling and increased salinity in the
77 subsurface layer, accompanied by an upward shift of the 20°C isotherm, a decrease in heat and kinetic
78 energy (Lin et al., 2005; Liu et al., 2017; Huang and Wang, 2022). Lu et al. (2020) proposed that typhoons
79 primarily generate potential vorticity input through the geostrophic response. When a typhoon passes
80 over an eddy, there is a significant positive wind stress curl within the typhoon's maximum wind radius,
81 which induces upwelling in the mixed layer due to the divergence of the wind-driven flow field. This
82 upward flow compresses the thickness of the isopycnal layers below the mixed layer, resulting in a
83 positive potential vorticity anomaly. By analyzing the time series of ocean kinetic energy, available
84 potential energy (APE), vorticity budget, and potential vorticity (PV) budget, Rudzin and Chen (2022)
85 found that the positive vertical vorticity advection caused the TC to eliminate the warm eddy from bottom
86 to top after passing through. Under the interaction of the strong TC wind stress in the eye area of the
87 typhoon and the subsurface ocean current field, the early-onset of a near-inertia wake caused the
88 disappearance of the warm eddy. However, the projection of TC wind stress onto the eddy and the relative



89 position of the warm eddy to the typhoon can lead to different responses. According to the classical
90 description of TC-induced upwelling, strong upwelling occurs within twice the maximum wind radius
91 of the typhoon center, while weak subsidence exists in the vast area outside the upwelling region (Price,
92 1981; Jullien et al., 2012). The warm eddy located directly beneath the typhoon's path weakens due to
93 the cold suction caused by the typhoon's center. However, for warm eddies located beyond twice the
94 maximum wind radius, they are influenced by the typhoon's wind stress curl and the downwelling within
95 the eddy itself, resulting in the convergence of warm water in the upper layers of the eddy, an increase
96 in mixed layer thickness, and an increase in heat content, leading to a warming response to the typhoon
97 (Jaimes and Shay, 2015).

98 Previous studies on the interaction between warm eddies and typhoons have primarily focused on the
99 enhancing impact of warm eddies on typhoons. However, there has been relatively limited exploration
100 of different responses exhibited by warm eddies under the influence of typhoons. In this study, in-situ
101 measurements, remote sensing data, and GLORYS12V1 reanalysis data are utilized to investigate distinct
102 responses of two warm eddies to typhoon Kalmaegi in the NSCS. Section 2 provides an overview of the
103 data and methods utilized in this research. Section 3 analyzes the physical parameters of warm eddies,
104 vertical temperature and salinity variations, and explores the different responses of warm eddies both
105 inside and outside the typhoon affected region. Section 4 offers a comprehensive discussion and Section
106 5 gives a summary.

107 **2. Data and Methods**

108 **2.1. Data**

109 The six-hourly best-track typhoon datasets were obtained from the Joint Typhoon Warning Center
110 (JTWC, <http://www.usno.navy.mil/JTWC>, last access: 3 February, 2021), the Japan Meteorological
111 Agency (JMA, <https://www.jma.go.jp/jma/jma-eng/jma-center/rsmc-hp-pub-eg/besttrack.html>, last
112 access: 3 February, 2021), and the China Meteorological Administration (CMA, <http://tcdata.typhoon.gov.cn>, last access: 3 February, 2022). The data contained the tropical cyclone
113 center locations, the minimum central pressure, maximum sustained wind speed, and intensity category.
114 The translation speed of typhoons was calculated by dividing the distance travelled by each typhoon
115 within a 6-hour interval by the corresponding time. In this paper, typhoon Kalmaegi and tropical storm
116 Fung-wong were studied (Fig. 2).

118 The daily Sea Level Anomaly (SLA) and geostrophic current data provided by Archiving, Validation,
119 and Interpretation of Satellite Data in Oceanography (AVISO) product (CMEMS,



120 <https://marine.copernicus.eu/>, last access: 14 February, 2022). This dataset combines satellite data from
121 Jason-3, Sentinel-3A, HY-2A, Saral/AltiKa, Cryosat-2, Jason-2, Jason-1, T/P, ENVISAT, GFO, and
122 ERS1/2. The spatial resolution of the product is $1/4^\circ \times 1/4^\circ$, the period from 1 September to 30 September
123 2014 was used.

124 The daily Sea Surface Temperature (SST) data used in this study is derived from the Advanced Very
125 High Resolution Radiometer (AVHRR) product data provided by the National Oceanic and Atmospheric
126 Administration (NOAA). The data is obtained from the Physical Oceanography Distributed Active
127 Archive Center (PODAAC) at the NASA Jet Propulsion Laboratory (JPL)
128 (http://podaac.jpl.nasa.gov/documents/dataset_docs/avhrr_pathfinder_sst.html), last access: 16 March,
129 2022). The spatial resolution of the data is $1/4^\circ \times 1/4^\circ$.

130 Argo data, including profiles of temperature and salinity from surface to 2000 m depth are obtained
131 from the real-time quality-controlled Argo data base (Euro-Argo, <https://dataselection.euro-argo.eu/>, last
132 access: 4 April, 2022). We selected Argo float number 2901469, situated in an ocean anticyclonic eddy
133 and in close proximity to typhoon Kalmaegi, both before and after the typhoon's passage in 2014. Profiles
134 of this Argo were also used to validate the vertical distribution of temperature and salinity from
135 GLORYS12V1.

136 For this study, we also utilized in situ data from a cross-shaped array consisting of five stations,
137 comprising five moored buoys and four subsurface moorings (refer to Fig. 2). More specific information
138 can be found in Zhang et al. (2016). To investigate the impact of the typhoon on a warm eddy, we selected
139 the temperature and salinity data from Station 5, situated along the left track of Kalmaegi.

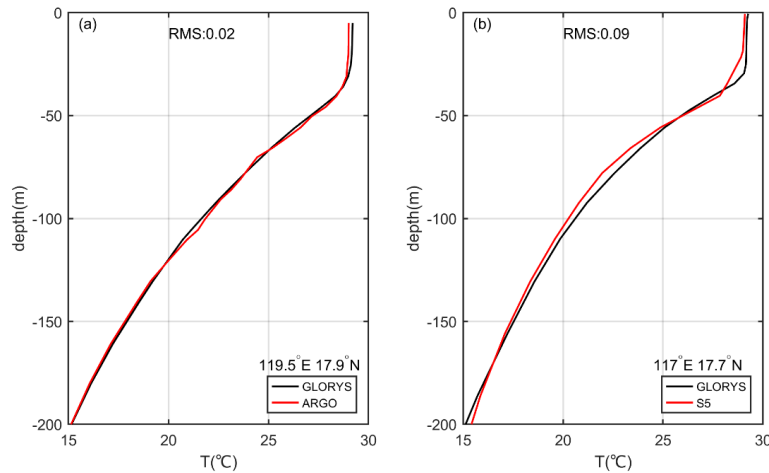
140 The wind speed data was sourced from the European Centre for Medium-Range Weather Forecasts
141 (ECMWF) ERA-Interim reanalysis assimilation dataset ([https://apps.ecmwf.int/datasets/data/interim-
142 full-daily/levtype=sfc/](https://apps.ecmwf.int/datasets/data/interim-full-daily/levtype=sfc/)), last access: 5 January, 2023). This dataset was widely used for weather analysis
143 and numerical forecasting. The wind field data used in this study primarily focused on the reanalysis data
144 of surface winds at a height of 10 meters above sea level for tropical cyclones. The selected data had a
145 spatial resolution of $1/4^\circ \times 1/4^\circ$ and a temporal resolution of 6 hours, with four updates per day (00:00,
146 06:00, 12:00, and 18:00 UTC). The data utilized corresponds to September 2014.

147 The Global Ocean Reanalysis Product GLOBAL_REANALYSIS_PHY_001_030 (GLORYS12),
148 provided by the Copernicus Marine Environment Monitoring Service (CMEMS,
149 <https://marine.copernicus.eu/>, last access: 23 March, 2022) was used in this study too. This reanalysis
150 product utilized the NEMO 3.1 numerical model coupled with the LIM2 sea ice model, and forced with
151 ERA-Interim atmospheric data. The model assimilated along-track altimeter data from satellite
152 observations (Pujol et al., 2016), satellite sea surface temperature data from AVHRR, sea ice
153 concentration from CERSAT (Ezraty et al., 2007), and vertical profiles of temperature and salinity from
154 the CORAv4.1 database (Cabanes et al., 2012). The temperature and salinity biases were corrected using
155 a 3D-VAR scheme. The horizontal resolution is $1/12^\circ \times 1/12^\circ$, and it has 50 vertical levels. The
156 temperature and salinity during 1 September to 30 September 2014 was chosen to study.

157 GLORYS12V1 is a widely used and applicable dataset, to evaluate its temperature profiles, the Argo
158 profiles and in-situ data of Station 5 were compared (Fig. 1). The GLORYS12V1 data exhibit good



159 agreement with Argo profiling floats, the maximum difference between them is less than 0.2°C. However,
 160 there are some discrepancies between the GLORYS12V1 and the Station 5 data, with the largest
 161 difference occurring at the depths of 30 m (mixed layer) and 78 m (thermocline), both differing by 0.6°C,
 162 while below 150 m, the difference is quite small. This may be because the vertical resolution of upper
 163 100 m in Argo profile is 5 m, but the vertical interval of Station 5 is 20 m, it is sparser. Therefore, the
 164 large deviations exist at mixed layer and thermocline during the typhoon in in-situ data of Station 5.
 165 Overall, GLORYS12V1 reproduces the observed ocean temperature accurately, it is reasonable to use it
 166 to investigate the vertical feedback of the ocean by typhoon Kalmaegi.



167
 168 **Figure 1.** Evaluation of GLORYS12V1 data performance during September 2014. **(a)** Vertical monthly mean
 169 temperature within the anticyclonic eddy AE2 (119.5°E 17.9°N) as measured by Argo float 2901469. **(b)**
 170 Comparison of vertical monthly mean temperature recorded at Station 5 (117°E 17.7°N).

171 **2.2. Methods**

172 Vorticity is a vector that characterizes the local rotation within a fluid flow. Mathematically, it is
 173 defined as the curl of the velocity vector. In most cases, when referring to vorticity, it specifically pertains
 174 to the vertical component of the vorticity. It is calculated from:

175
$$\zeta = \frac{\partial v}{\partial x} - \frac{\partial u}{\partial y} . \tag{1}$$

176 u and v are the zonal (eastward) and meridional (northward) geostrophic velocities, respectively. They
 177 are derived from altimeter sea level anomaly data (η):

178
$$u = -\frac{g}{f} \frac{\partial \eta}{\partial y} , v = \frac{g}{f} \frac{\partial \eta}{\partial x} . \tag{2}$$

179 Here, g is the acceleration of gravity, f is the Coriolis frequency. Vorticity is considered a
 180 fundamental characteristic of mesoscale eddies, positive vorticity signifies cyclonic eddies, while
 181 negative vorticity indicates anticyclonic eddies.



182 The Rossby number (Ro) is a dimensionless number describing fluid motion, and it is the ratio of
183 relative vorticity to planetary vorticity, reflecting the relative importance of local non-geostrophic motion
184 to large-scale geostrophic motion. The larger the Rossby number, the stronger the local non-geostrophic
185 effect, and the definition of this parameter is:

$$186 \quad Ro = \frac{\zeta}{f} . \quad (3)$$

187 Eddy Kinetic Energy (EKE) is a measure of the energy associated with mesoscale eddies, which
188 indicates the intensity of eddies. It is typically calculated using the anomalies of the geostrophic velocity:

$$189 \quad EKE = \frac{1}{2} (u'^2 + v'^2) , \quad (4)$$

190 where u' represents the anomaly of the geostrophic zonal (eastward) velocity, v' represents the anomaly
191 of the meridional (northward) velocity.

192 To evaluate the impact of a typhoon on an anticyclonic eddy, the calculation begins with determining
193 the wind stress:

$$194 \quad \vec{\tau} = \rho_a C_d U_{10} \vec{U}_{10} , \quad (5)$$

195 where ρ_a is the air density, assumed to be a constant value of 1.293 kg m^{-3} , U_{10} represents the 10-
196 meter wind speed. And C_d is the drag coefficient at the sea surface (Oey et al., 2006):

$$197 \quad C_d \times 1000 = \begin{cases} 1.2 & U_{10} \leq 10 \text{ m s}^{-1} \\ 0.49 + 0.65 U_{10} & 11 \leq U_{10} < 19 \text{ m s}^{-1} \\ 1.364 + 0.234 U_{10} - 0.00023158 U_{10}^2 & 19 \leq U_{10} \leq 100 \text{ m s}^{-1} \end{cases} . \quad (6)$$

198 The wind stress curl is calculated by (Kessler, 2006):

$$199 \quad \text{curl}(\vec{\tau}) = \frac{\partial \tau_y}{\partial x} - \frac{\partial \tau_x}{\partial y} , \quad (7)$$

200 where τ_x and τ_y are the eastward and northward wind stress vector components, respectively. The curl
201 represents the rotation experienced by a vertical air column in response to spatial variations in the wind
202 field.

203 The Ekman pumping velocity (EPV) represents the ocean upwelling rate, which can be used to study
204 the contribution of typhoons to regional ocean upwelling. Positive means upwelling, negative represents
205 downwelling:

$$206 \quad EPV = \text{curl}\left(\frac{\vec{\tau}}{\rho f}\right) , \quad (8)$$

207 where the wind stress is obtained from Eq. (7), ρ is seawater density, the value is 1025 kg m^{-3} , and f
208 is the Coriolis frequency.

209 The buoyancy frequency is a measure of the degree to which water is mixed and stratified. In a stable
210 temperature stratification, the fluid particles move in the vertical direction after being disturbed, and the
211 combined action of gravity and buoyancy always makes them return to the equilibrium position and
212 oscillate due to inertia. The frequency of oscillation is the floating frequency (N). When $N^2 < 0$, the



213 water is in an unstable state. The larger N is, the lower the degree of mixing and the higher the degree of
214 stratification:

$$215 \quad N = \sqrt{-\frac{g}{\rho} \frac{\partial \rho}{\partial z}} \quad (9)$$

216 Where ρ is seawater density, g is the acceleration of gravity, and z is the depth.

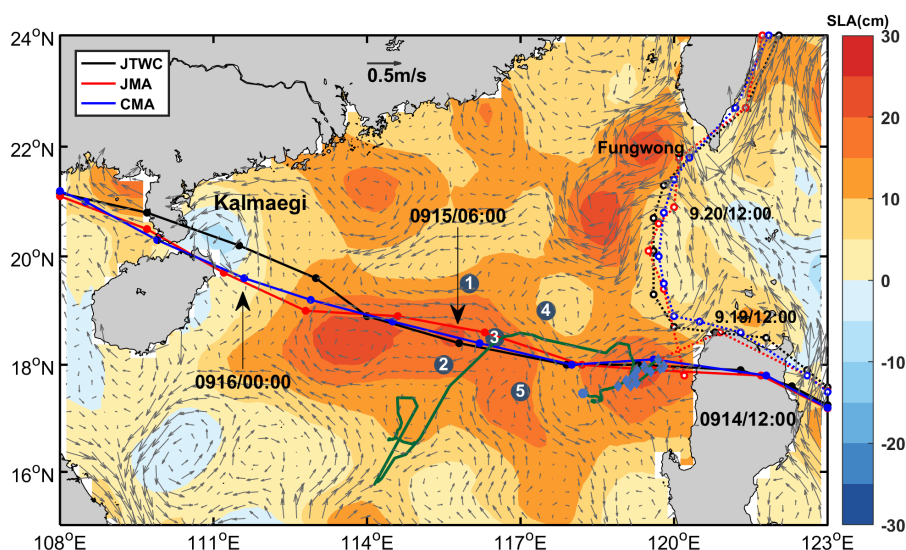
217 3. Results

218 3.1. Typhoon and pre-existing eddies in the NSCS

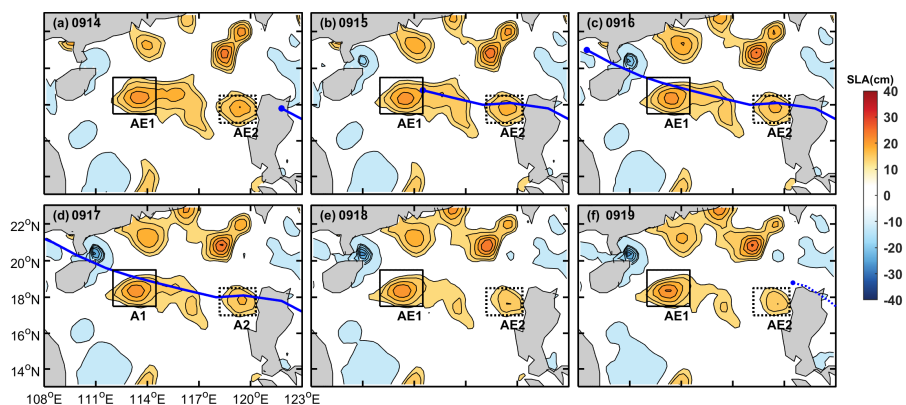
219 3.1.1. Track of typhoon Kalmaegi and tropical storm Fung-wong

220 Tropical cyclone Kalmaegi strengthened into a typhoon by 1200 UTC on 13 September and emerged
221 over the warm waters of the Northern South China Sea (NSCS) by 1500 UTC on 14 September, with
222 maximum sustained winds of 33 m s^{-1} (Fig. 2-3). During this period, the NSCS experienced
223 predominantly weak wind shear (Fig. 4a) and was characterized by multiple anticyclonic warm eddies
224 (Fig. 2). Subsequently, typhoon Kalmaegi underwent two rapid intensification phases between 15 and
225 16 September (Fig. 4c-f). The first intensification occurred at 0000 UTC on 15 September, propelling
226 Kalmaegi to category 1 status with surface winds surpassing 35 m s^{-1} . By 1200 UTC on 15 September,
227 Kalmaegi experienced a second, even more rapid intensification, with winds reaching 40 m s^{-1} in less
228 than 12 hours. Throughout this intensification stage, Kalmaegi encountered two warm eddies:
229 anticyclonic eddy AE1, located to the left of the typhoon's path (Fig. 3), which had a lifespan of 105 days
230 from 26 June to 8 October and was positioned at 17°N - 20°N , 113°E - 116°E , and AE2, precisely
231 intersecting with the typhoon's trajectory, which had a lifespan of 89 days from 24 August to 20
232 November and was located at 17°N - 19°N , 118°E - 120°E . Kalmaegi made landfall on Hainan Island at
233 0300 UTC on 16 September, with a minimum central pressure of 960 hPa and maximum wind speed of
234 40 m s^{-1} . After landfall, Typhoon Kalmaegi gradually weakened and dissipated. During it across the
235 NSCS, the five mooring stations were affected. Stations 1 and 4 were on the right side of Typhoon
236 Kalmaegi's track, while Stations 2 and 5 were on the left side. Unfortunately, the wire rope of the buoy
237 at Station 3 was destroyed by Kalmaegi, resulting in missing data from 15 September. Among the stations,
238 Station 5 is on the left of typhoon track and outside AE2, so its data is used in our study.

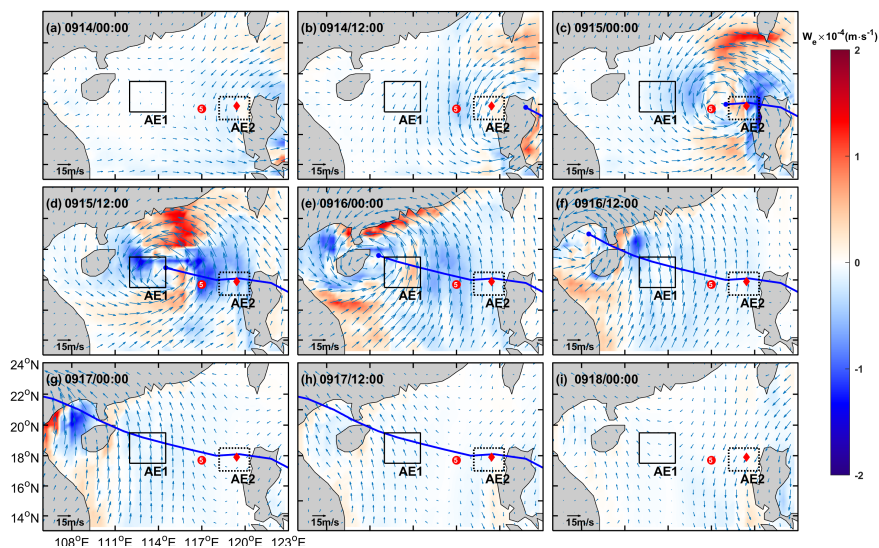
239 Tropical storm Fung-wong initially moved quickly in a northwest direction after formation. On 19
240 September, it entered the Luzon Strait and slowed down. It made landfall in Taiwan on the 21 September
241 and subsequently landed in Zhejiang on the 22 September before gradually dissipating. When crossing
242 the Luzon Strait at 1200 UTC on 19 September, anticyclonic eddy AE2 was on the left side of Fung-
243 wong with a distance of just over 100 km from its centre.



244
 245 **Figure 2.** The tracks of typhoon Kalmaegi (solid lines with dots) and tropical storm Fung-wong (dashed lines with
 246 hollow dots) as provide by the Joint Typhoon Warning Center (JTWC, black), Japan Meteorological Agency (JMA,
 247 red), and China Meteorological Administration (CMA, blue). The colour shading represents the sea surface level
 248 anomaly on 13 September, 2014, while the gray arrows illustrate the geostrophic flow field. The numbered blue dots
 249 represent the positions of the five buoy/mooring stations, the green line illustrates the trajectory of Argo 2901469,
 250 and the blue diamonds mark the positions of Argo 2901469 inside the eddy AE2 from 26 August 2014 to 25 October
 251 25, 2014.



252
 253 **Figure 3.** The variations in sea level anomaly before and after typhoon Kalmaegi moved over the anticyclonic eddies
 254 AE1 and AE2 between 14 September and 19 September (a-f). The black solid rectangle represents the area of AE1,
 255 while the black dashed rectangle represents the area of AE2. The blue solid line depicts the path of typhoon Kalmaegi,
 256 while the blue dotted line in (f) is the path of tropical storm Fung-wong (best-track data sourced from CMA).



257

258

259

260

Figure 4. Ekman Pumping Velocity (EPV) from 14 September to 18 September (a-i). The color represents the EPV, the blue solid line is the path of Kalmaegi, the red dot and diamond are the positions of Station 5 and Argo 2901469 on 15 September, respectively.

261

3.1.2. Eddy characteristics distribution

262

263

264

265

266

267

268

269

270

271

272

273

274

Satellite SLA measurements have proven to be highly effective and widely used for identifying and quantifying the intensity of ocean eddies (Li et al., 2014). In Fig. 3, two warm eddies with clear positive (>13 cm) SLA are observed along the typhoon Kalmaegi's track. During the period of 15 to 16 September, the typhoon passed over two warm anticyclonic eddies, AE1 and AE2. Before typhoon, AE1 is the most prominent eddy in the SCS, with an amplitude of 23.0 cm, and a radius of 115.5 km. AE2, located west of Luzon Island, exhibits an amplitude of 21.2 cm, with a radius of approximately 65.5 km. Tracing back to 2 months (figure is not shown), AE1 propagated slowly westward with about 0.1 m s^{-1} , while AE2 was generated on 24 August. During 14 to 19 September, the amplitude of AE1 increased 1.3 cm. The area of the AE1 decreased by approximately 31% from $1.3 \times 10^5 \text{ km}^2$ to $9.1 \times 10^4 \text{ km}^2$ and split into two eddies. When typhoon Kalmaegi crossed the core of AE2 at 1500 UTC on 14 September, and tropical storm Fung-wong moved over the northeast of AE2 at 1200 UTC on 19 September, the amplitude decreased by 3.1 cm. The area of the AE2 decreased by approximately 36% from $4.2 \times 10^4 \text{ km}^2$ to $2.7 \times 10^4 \text{ km}^2$. After 19 September, the influence of the typhoon on the warm eddies gradually diminished.

275

276

277

278

279

280

Because of intense solar radiation in September, the SST in the South China Sea was generally above 28.5°C prior to the arrival of typhoon Kalmaegi (Fig. 5a). As a fast-moving typhoon, the mean moving speed of typhoon Kalmaegi over 8 m s^{-1} , the cooling area and intensity on the right side of the path are larger compared to the left side (Price, 1981). During the passgae of Kalmaegi, the lowest SST on the right side of typhoon decreased to 27.2°C . Even after the typhoon has passed, a cold wake can still be observed on the right side of the path, persisting for over a week (Fig. 5c).



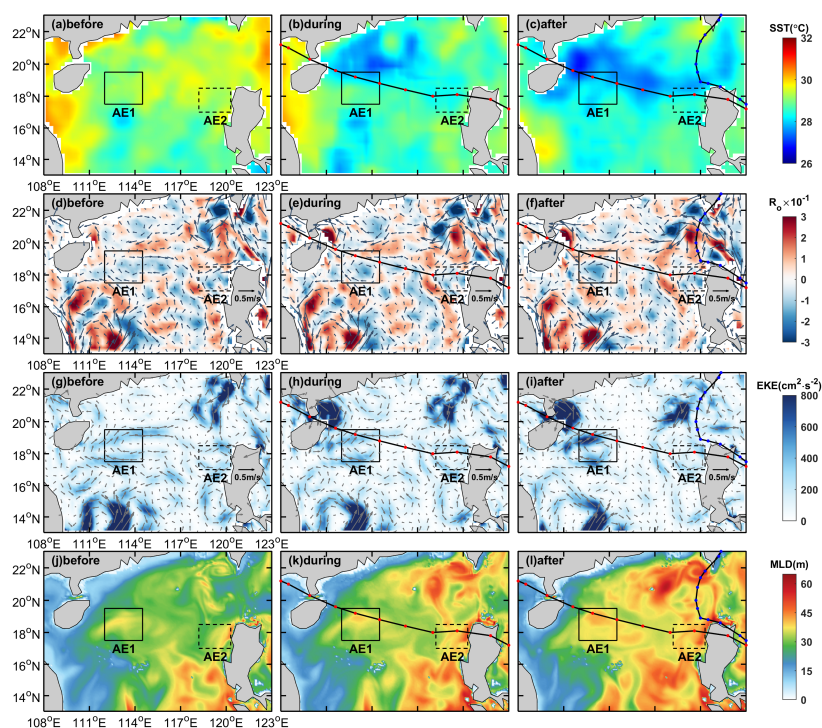
281 Mesoscale eddies, due to their special thermodynamic structure and varying positions in relation to
282 the typhoon, can modulate distinct sea surface temperature changes and exhibit different characteristics.
283 The pre-existing warm eddy AE1 began to cool down before the typhoon reached the NSCS, dropping
284 to 28.4°C on September 14. Meanwhile, the Ekman Pumping Velocity (EPV) was very small, smaller
285 than $0.5 \times 10^{-5} \text{ m s}^{-1}$ in both AE1 and AE2. During 15-16 September (Fig. 4c-f), when the typhoon
286 traversed the NSCS, the EPV experienced significant changes, the EPV increased to over $1.5 \times 10^{-4} \text{ m s}^{-1}$
287 within AE1 and AE2. The positive EPV contributed to the influx of colder subsurface water into the
288 upper layers, resulting in surface water cooling, while the negative EPV facilitated downwelling and
289 strengthened the influence of the warm eddies (Jaimes and Shay, 2015), during this period, the mean
290 SST within AE1 increased slightly to 28.6 °C (Fig. 6a). However, as cooler water from the right side of
291 the typhoon track was subsequently advected into the AE1 region (Fig. 5c), the SST decreased and
292 reached 28.0 °C on September 19, which was 0.4°C lower than that before the typhoon. The average sea
293 temperature drop in AE2 was relatively evident, with SST starting to decline before September 14 and
294 reaching its lowest point of 28.1°C on September 15, which was 0.6 °C lower than that before the typhoon
295 (Fig. 6e). On 16 September, the SST within AE2 began to recover, but it started to cool again on 18
296 September due to the influence of Fung-wong.

297 Then we compared the Rossby number (Ro) and EKE of AE1 and AE2 before, during and after
298 typhoon. Before being influenced by the typhoon, the warm eddy AE1 exhibited a more scattered
299 distribution of negative Ro due to its edge structure, and the EKE values at the eddy boundary were
300 relatively high (Fig. 5d, g). As the typhoon passed through the eddy, the Ro and EKE of AE1 started to
301 increase. On 19 September, the average Ro within AE1 reached a value of -8.2×10^{-2} , at the same time,
302 the average EKE increased to its maximum value of $325.0 \text{ cm}^2 \text{ s}^{-2}$. It can be observed that the variation
303 trend of Ro and EKE within the eddy is consistent, increasing from the passage of the typhoon and
304 starting to recover on 20 September (Fig. 6b-c). This indicates that although the area of the warm eddy
305 AE1 decreased under the influence of the typhoon, its intensity increased. On the other hand, for warm
306 eddy AE2, the Ro and EKE both decreased after the typhoon passage, with the Ro decreasing to -4.5×10^{-2}
307 on 17 September and the EKE decreasing to $152.0 \text{ cm}^2 \text{ s}^{-2}$ on the 19 September, followed by a recovery
308 (Fig. 6f-g). Unlike AE1, AE2 weakened in intensity under the influence of the typhoon.

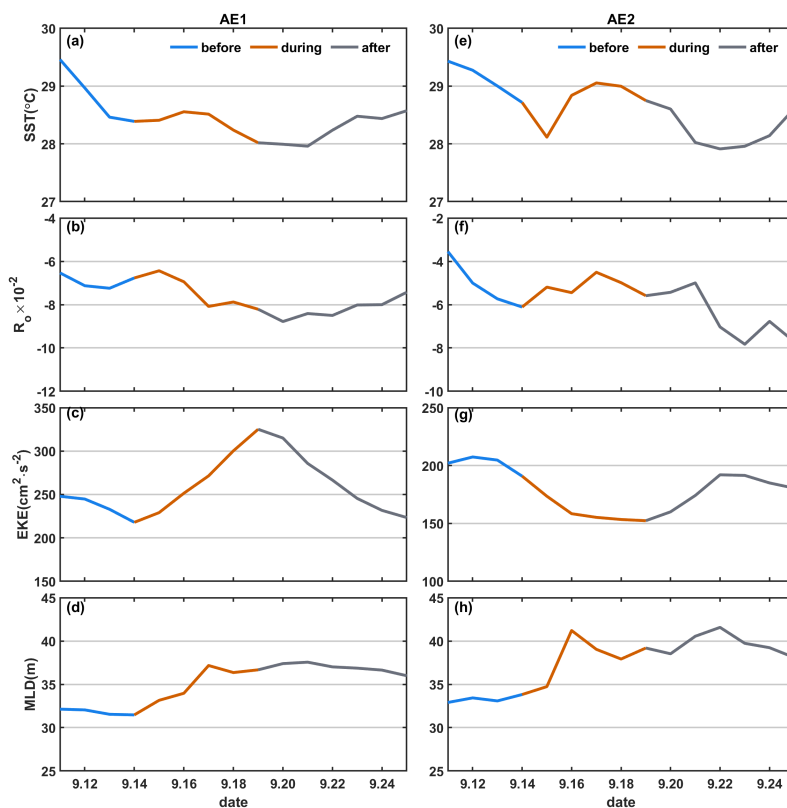
309 During the passage of the typhoon, the enhanced mixing driven by wind stress and increased vertical
310 shear result in a deepening of the mixed layer depth (MLD), which further strengthens the mixing
311 between the deep cold water and the upper warm water (Shay and Jaimes, 2009). To avoid a large part
312 of the strong diurnal cycle in the top few meters of the ocean, 10 m was set as the reference depth (De
313 Boyer Montégut, 2004). A 0.5 °C threshold difference from 10 m depth was calculated and defined as
314 the MLD (Thompson and Tkalic, 2014). Prior to the typhoon passage, the MLD in the AE1 and AE2
315 regions is deeper (Fig. 5j), the average MLDs of AE1 and AE2 are 32 m and 33 m, respectively. Starting
316 from September 14th, the MLDs were influenced by typhoon Kalmaegi, with the MLD of AE1 deepening
317 to 37 m and that of AE2 increasing to 41 m, representing a deepening of 5 m and 8 m, respectively (Fig.
318 6d, f). At the same time, the MLD on the right side of the typhoon track is also increasing, and the SST
319 in the corresponding area also drops significantly (Fig. 5l).



320 Overall, typhoon Kalmaegi likely exerted distinct impacts on the two warm eddies. Despite both AE1
 321 and AE2 experiencing a decrease in their respective areas by approximately one-third, and are
 322 accompanied by deepening of the MLD, the amplitude of sea level anomaly (SLA) within AE1 increased
 323 by 1.3 cm, whereas AE2 witnessed a decrease of about 3.1 cm in its amplitude. Furthermore, the sea
 324 surface temperature (SST), Rossby number and eddy kinetic energy (EKE) within AE1 and AE2
 325 exhibited contrasting patterns. In the following sections, we will delve into the underlying reasons behind
 326 these divergent responses of the two eddies to Typhoon Kalmaegi.



327
 328 **Figure 5.** The spatial distribution of SST, R_o , EKE, and MLD before, during and after the passage of typhoon
 329 Kalmaegi. The time periods of 10-13, 15-16 and 19-22 September are designated as stages before, during and after
 330 typhoon, respectively. The path of typhoon Kalmaegi is depicted by a black solid line with red dots, while the path
 331 of tropical storm Fung-wong is represented by a black solid line with blue dots in the third column. The solid and
 332 dashed boxes correspond to AE1 and AE2, respectively.



333

334 **Figure 6.** The time series of sea surface temperature (SST), R_0 , eddy kinetic energy, and mixed layer depth (MLD)
 335 within the warm eddies' regions (black solid and dashed boxes in Fig. 5). The first column is variables of AE1, the
 336 second column is AE2.

337 3.2 Upper-ocean vertical thermal and salinity structure of eddies

338 We conducted further analysis on the vertical temperature and salinity structure of the warm eddies
 339 AE1 and AE2 before and after the typhoon Kalmaegi using GLORYS12V1 data. Fig. 7 illustrates that
 340 during the typhoon's passage on 15 September, the temperature above the MLD within AE1 increased
 341 by approximately 0.1 °C, while the salinity decreased by 0.02psu. Below the MLD, the temperature
 342 showed a significant increase, reaching a maximum temperature rise of 1.3 °C. Correspondingly, the
 343 salinity below the MLD exhibited a decrease of 0.05 psu. These changes led to a deepening of the
 344 isodensity by 15 m and a decrease in buoyancy frequency N^2 (Fig. 8a-b), indicating convergence and
 345 downwelling within the centre of the warm eddy AE1 (Fig. 4c-d).

346 After 15 September, the temperature above the MLD decreased and the salinity show an increase
 347 (Fig. 7a-b), resulting in the uplift of the 1021 kg m⁻³ isodensity to the sea surface (Fig. 8a-b). The
 348 subsurface warming and salinity reduction gradually weakened after the typhoon Kalmaegi but persisted
 349 for about a week after the typhoon's passage until 22 September. This persistence can be attributed to
 350 the intensified stratification around MLD, with N^2 around $9.0 \times 10^{-4} \text{s}^{-2}$ (Fig. 8b). The increased stability

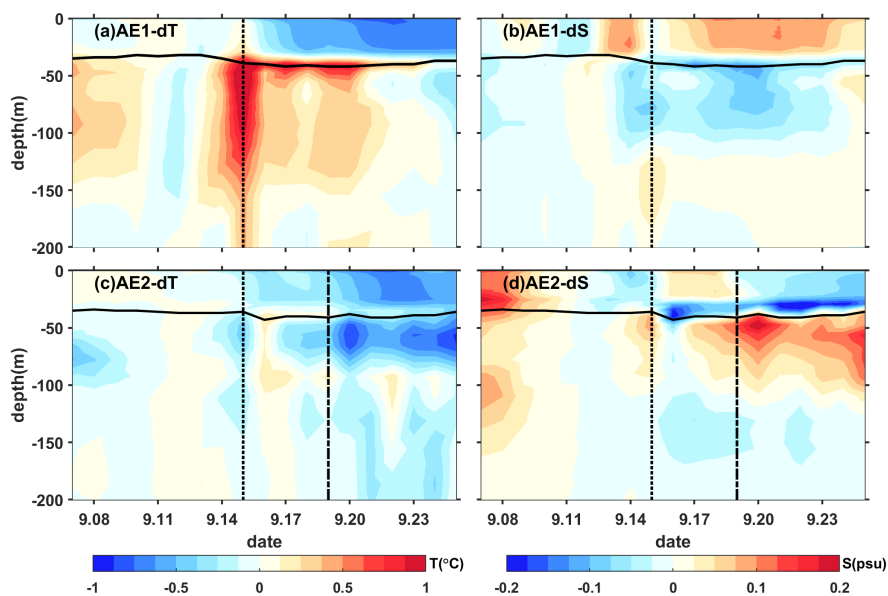


351 inhibits vertical mixing, restrains the exchange of heat and salinity, and leads to smoother density
 352 gradients above the MLD (Fig. 8a).

353 The vertical temperature and salinity structure of AE2 exhibit an opposite trend. During the typhoon
 354 passage on 15 September, AE2 also experienced a cooling trend of 0.2 °C, with a decrease in salinity of
 355 0.04psu above the MLD. Below the MLD, the temperature showed a consistent decrease, with a change
 356 of less than 0.5 °C within the subsurface. Correspondingly, the salinity exhibited an increase of
 357 approximately 0.08 psu (Fig. 7c-d). The slightly upward shift of the isodensity (Fig. 8c) suggests the
 358 possibility of cold-water upwelling induced by the suction effect of the typhoon. The temperature
 359 decrease and salinity increase below the MLD were primarily driven by upwelling processes.

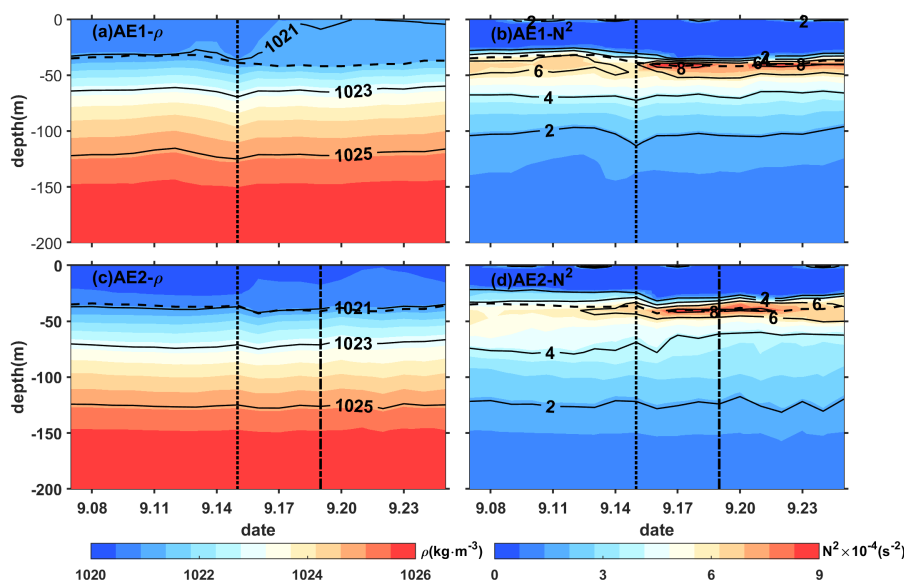
360 Furthermore, when the tropical storm Fung-wong passed through AE2 on 19 September (dashed line
 361 in Fig. 7c-d), the decreasing trend of subsurface temperature became more pronounced, and the
 362 subsurface salinity exhibited a significant increase. AE2 was more significantly influenced by the
 363 typhoon Fung-wong. This can be attributed to the presence of a stable stratification with N^2 around
 364 $8.4 \times 10^{-4} \text{s}^{-2}$ at a depth of 42 m, which created a barrier layer preventing the intrusion of high-salinity cold
 365 water from the lower layers into the mixed layer (Yan et al., 2017).

366



367

368 **Figure 7.** The timeseries of vertical temperature and salinity anomalies in the center of the warm eddies. The
 369 anomalies were calculated relative to the average value of 10-13 September. The vertical black dotted line
 370 indicates the typhoon Kalmaegi's passage, while the vertical black dashed line represents the passage of tropical
 371 storm Fung-wong. The black solid line is the MLD.



372

373 **Figure 8.** Same as Fig. 7, but for density and buoyancy frequency (N^2).

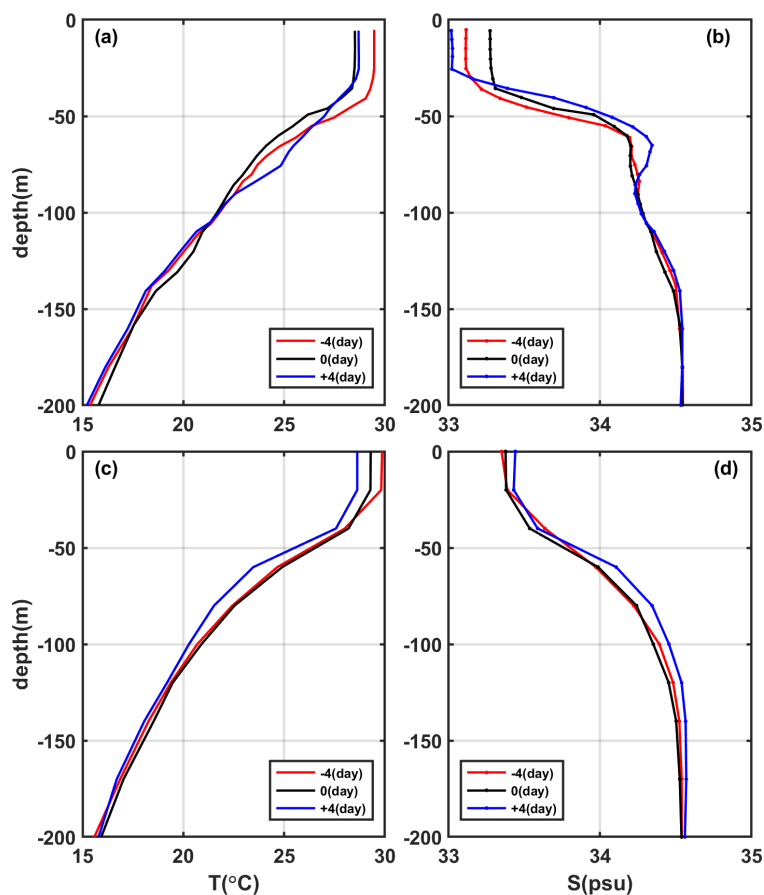
374 **3.3 Comparison of the response between eddies and non-eddies areas**

375 To investigate the contrasting response of warm eddies and the non-eddies background to typhoon
 376 Kalmaegi, we conducted a comparative analysis of vertical temperature and salinity profiles with these
 377 two areas. We examined data from Argo 2901469, which was located within AE2 during the period 11-
 378 19 September, while the temperature and salinity data from Station S5 was considered as the background,
 379 the S5 had a distance of 246 km from AE2's center on 15 September (Fig. 4). These profiles were
 380 categorized into three periods: pre-typhoon (11 September), during-typhoon (15 September), and post-
 381 typhoon (19 September).

382 At above 40m depth, both inside and outside of AE2 experienced a decrease in temperature, with a
 383 cooling of less than -1.0°C . Four days after the typhoon passage (19 September), the cooling persisted
 384 inside and outside the eddy, with the cooling being more pronounced outside the AE2, showing a
 385 decrease of 1.2°C (Fig. 9c). The salinity within AE2 initially increased by 0.15 psu from the pre-typhoon
 386 stage to the during-typhoon stage and then decreased by 0.09 psu after the typhoon passage (Fig. 9d). In
 387 contrast, the salinity at Station S5 showed a similar pattern on pre-typhoon and during-typhoon stage,
 388 but increased by 0.05 psu after the typhoon. Two possible processes can explain the difference in salinity
 389 trends. First, during the pre-typhoon to typhoon stage, the entrainment within AE2 may have brought the
 390 subsurface water, which is saltier, up to the surface, resulting in an increase in salinity. The second
 391 process is related to the typhoon-induced precipitation after the typhoon passage, which led to a decrease
 392 in salinity. Strong stratification could have contributed to the persistence of saltier subsurface water.
 393 While in the S5, the increase in salinity was relatively minor only increased slightly.



394 On 15 September, the subsurface layer at 45 m to 100 m was affected by the cold upwelling caused
395 by the typhoon, resulting in a cooling and increased salinity within the AE2 warm eddy. As the typhoon's
396 forcing diminished, the upper layer of seawater began to mix, and influenced by the downward flow of
397 the eddy itself, warm surface water was transported to the subsurface layer. Four days later, a warming
398 phenomenon occurred, with the maximum warm anomaly of 1.2 °C observed at a depth of 75 m (Fig.
399 9a). The mixing effect outside the eddy was not significant, resulting in a slight subsurface warming of
400 approximately 0.2 °C, with no significant changes in salinity. However, on 19 September, a cooling
401 center of -1.2°C was observed at a depth of 60 m, corresponding to the maximum salinity anomaly of
402 0.13 psu (Fig. 9c-d). Below 100 m, the AE2 warm eddy experienced a temperature increase of 0.5 °C
403 and a slight decrease in salinity of 0.04 psu. On 19 September, the temperature and salinity within the
404 AE2 eddy showed little change. However, outside the eddy, a different response was observed. On
405 September 19th, a cooling trend was observed throughout the water column, within a range of 0.2 °C,
406 accompanied by a noticeable increase in salinity (Fig. 9c, d), within a range of 0.06 psu. This indicates
407 that the typhoon caused a significant upwelling outside the eddy region.



408



409 **Figure 9.** (a-b) the vertical profile of temperature and salt inside the eddy (Argo 2901469), (c-d) the vertical profiles
410 of temperature and salt outside the eddy (S5). The red, black and blue lines represent pre-typhoon, during-typhoon
411 and post-typhoon stages.

412 Based on Argo profiles and S5 data, the upper ocean above 200 m inside and outside the eddy
413 responded differently to the forcing of the typhoon. In the upper layer (0-40m), cooling was observed
414 both inside and outside the eddy, and it lasted for a longer duration. In the subsurface layer (45-100m),
415 after the passage of the typhoon (19 September), there was a strong cooling outside the eddy, while
416 warming occurred within the warm eddy AE2. Zhang (2022) pointed out that the sea temperature
417 anomalies mainly depend on the combined effects of mixing and vertical advection (cold suction).
418 Mixing causes surface cooling and subsurface warming, while upwelling (downwelling) leads to cooling
419 (warming) of the entire upper ocean. The temperature anomaly in the subsurface layer depends on the
420 relative strength of mixing and vertical advection, with cold anomalies dominating when upwelling is
421 strong, and downwelling amplifying the warming anomalies caused by mixing. Therefore, due to the
422 strong influence of upwelling outside the eddy, the temperature profile of the entire water column shifts
423 upwards, resulting in cooling of the entire upper ocean. On the other hand, influenced by the downwelling
424 associated with the warm eddy itself, a warming anomaly of 1.2 °C is observed in the subsurface layer.
425 Compared to region AE2, the cold suction effect caused by the typhoon Kalmaegi is still evident in the
426 non-eddy area.

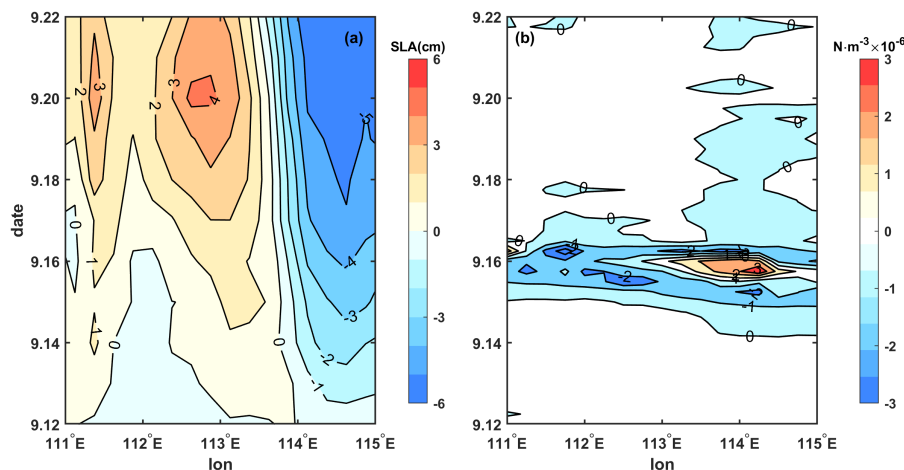
427 **4. Discussion**

428 From the above, the relative position of warm eddies and the typhoon can influence the response of
429 the eddies(Lu et al., 2020). The warm eddy AE1, located on the left side of the typhoon track, was not
430 weakened by the strong cold suction effect caused by the typhoon Kalmaegi. Instead, it was strengthened
431 due to the stronger negative wind stress curl generated by the typhoon. Starting from 15 September, there
432 was a significant positive sea level anomaly (SLA) to the west of 113.5°E, and its intensity increased,
433 reaching its maximum on 20 September (Fig. 10a). This strengthening is consistent with the increase in
434 the amplitude of the warm core of the eddy AE1. Comparing with the wind stress curl anomaly (Fig.
435 10b), it can be seen that from 15 to 16 September, the typhoon Kalmaegi moved over the section at
436 18.2°N, specifically to the west of 113.5°E, exhibited strong negative wind stress curl anomalies, with a
437 maximum intensity of $-3 \times 10^{-6} \text{ N.m}^{-3}$. The negative wind stress curl induced by the typhoon resulted in
438 favourable surface ocean currents that further enhanced the anticyclonic spin of the warm eddy. The
439 negative wind stress curl anomaly caused strong downwelling currents, inputting negative vorticity into
440 AE1, leading to its intensification (Fig. 6b-c), as indicated by the enhanced positive SLA (Fig. 10a).
441 Conversely, the region to the east of 113.5°E along the section exhibited negative SLA anomalies. This
442 weakening is consistent with the previous observations of the intensified warm core and decreased eddy
443 area in the eddy AE1.

444 Comparing with the wind stress curl anomaly (Fig. 10b), it can be seen that from 15-16 September,
445 there is a strong positive wind stress curl anomaly at the center section of AE1, specifically at 114°E,



446 with a maximum intensity of $3 \times 10^{-6} \text{ N m}^{-3}$. The positive wind stress curl induces upwelling, which inputs
 447 the positive vorticity of the typhoon-induced wind stress curl downward into the eddy (Huang and Wang,
 448 2022), corresponding to the decrease in SLA (Fig. 10a).



449
 450 **Figure 10.** The time/longitude plots of (a) SLA anomaly (cm) and (b) wind stress curl (N.m^{-3}) anomaly at the central
 451 section of AE1 (18.2°N). The anomalies were calculated relative to the average value of 10-13 September.

452 The response of the warm eddy AE2 is different from AE1 mainly because AE2 is quite near the
 453 typhoon track, and the significantly positive wind stress curl at the center of the typhoon noticeably
 454 weakens the eddy. Furthermore, based on the meridional isotherm profiles of the eddy center at three
 455 periods, it can be observed that during the passage of Typhoon Kalmaegi (15 September), the isotherms
 456 in the AE1 region exhibit significant subsidence (Fig. 11a), while in the AE2 region, the isotherms show
 457 uplift (Fig. 11b). This result is consistent with the earlier finding that the convergence and subsidence
 458 within the warm eddy AE1 are enhanced by the influence of the wind stress curl induced by the typhoon,
 459 while the intensity of AE2 is weakened.

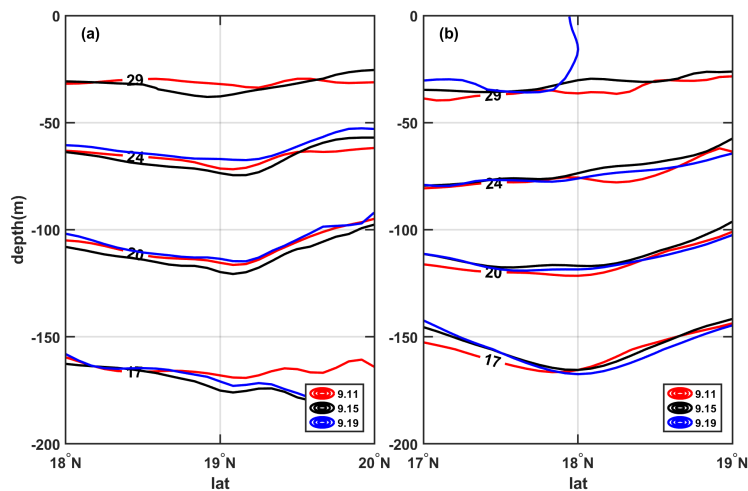
460 To understand the work done by the typhoon on the eddy in the ocean, we estimate the total work
 461 inputted into the ocean current u_c using the previously calculated wind stress (Liu et al., 2017):

462
$$W = \int \vec{\tau} \cdot \vec{u}_c dt . \quad (10)$$

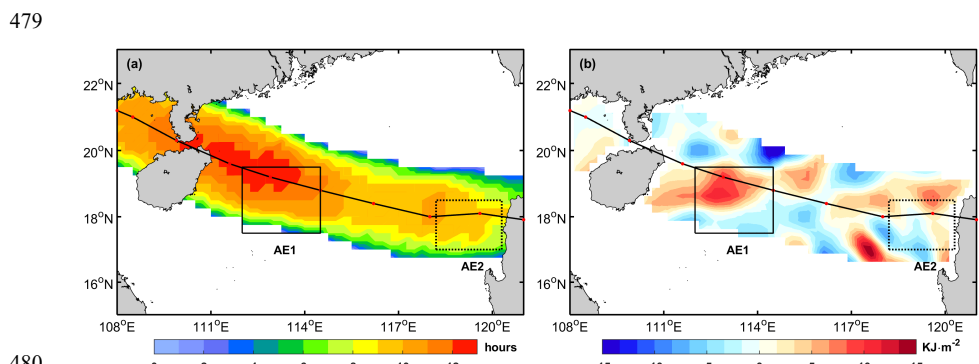
463 Here, we select the region near the typhoon track where the wind speed is greater than 17 m.s^{-1} as the
 464 typhoon forcing region to understand the energy inputted by the typhoon to the warm eddy (Sun et al.,
 465 2010). The forcing duration over the ocean in the typhoon-affected region and the work done by the
 466 typhoon on the surface current are shown in Fig. 12. When the angle between the wind and the ocean
 467 current is acute, the typhoon does positive work on the ocean current. Conversely, when the angle is
 468 obtuse, the typhoon does negative work on the ocean current. It can be observed that the region with the
 469 maximum forcing duration by the typhoon on AE1 is also the area where the typhoon clearly does
 470 positive work on the ocean current, with a cumulative work done exceeding 8 KJ m^{-2} . This accelerates
 471 the flow velocity in the eddy, resulting in convergence within the eddy and an increase in SLA, leading
 472 to the strengthening of AE1. On the other hand, the forcing duration by the typhoon on AE2 is smaller,



473 and the typhoon does negative work on the ocean current in most areas, with a cumulative work done
 474 within -5 KJ m^{-2} , causing the flow velocity within the AE2 to decelerate. The center height decreases and
 475 AE2 weakens.



476
 477 **Figure 11.** The meridional isotherm profiles of AE1 (a) and AE2 (b) before (11 September), during (15 September)
 478 and after (19 September) typhoon Kalmaegi,



480
 481 **Figure 12.** (a): the forcing time (unit: hours) of the typhoon; (b): the input work (unit: $\text{KJ} \cdot \text{m}^{-2}$) of the typhoon to
 482 the current.

483 5. Summary

484 Based on multi-satellite observations, on-site measurements, and numerical model data, we have
 485 gained valuable insights into the response of warm eddies AE1 and AE2 in the northern South China Sea
 486 to Typhoon Kalmaegi. Both horizontally and vertically, these eddies displayed distinct differences.
 487 Horizontally, we observed a reduction in their respective areas by approximately 31% (AE1) and 36%
 488 (AE2). AE1, positioned on the left side of the typhoon's track, strengthened with amplitude, R_o and EKE
 489 increasing by 1.3 cm, 1.4×10^{-2} and $107.2 \text{ cm}^2 \text{ s}^{-2}$ after the typhoon passed. In contrast, AE2, which
 490 intersected with the typhoon's track, weakened with amplitude, R_o and EKE decreasing by 3.1 cm,



491 1.6×10^{-2} and $38.5 \text{ cm}^2 \text{ s}^{-2}$, respectively. Vertically, during the typhoon's passage, AE1 experienced
492 intensified converging subsidence flow at its center, leading to an increase in temperature and a decrease
493 in salinity above depth of 150m. This response was more pronounced below the MLD (1.3°C) and
494 persisted for about a week after the typhoon. On the other hand, AE2 exhibited cooling above the MLD,
495 accompanied by a decrease in salinity, as well as a subsurface temperature drop and salinity increase due
496 to the upwelling of cold water caused by the typhoon's suction effect. The subsurface cooling and salinity
497 increase in AE2 were further influenced by Typhoon Fung-wong. Additionally, from the temperature
498 vertical profile of Argo and in-situ arrays, on 19 September, it can be seen that the non-eddy region also
499 experienced significant cooling, with a prominent cooling center observed at a depth of 60 m (-1.2°C).
500 The warm eddy AE2, influenced by its own downwelling, exhibited enhanced mixing effects, resulting
501 in a subsurface warm anomaly of 1.2°C .

502 Further analysis reveals that the different responses of the warm eddies can be attributed to factors
503 such as wind stress curl distribution, which are influenced by the relative position of the warm eddies
504 and the typhoon track. The wind stress curl induced by the typhoon plays a crucial role in shaping the
505 response of the warm eddies. AE1, located on the left side of the typhoon's path, experienced prolonged
506 forcing from the typhoon, resulting in positive work on the ocean current. This inputted a strong negative
507 wind stress curl into the eddy, enhancing negative EPV, so the downwelling within the AE1 is obvious
508 and contributing to its increased strength. In contrast, AE2, positioned directly below the typhoon's track,
509 experienced shorter forcing duration and weakened due to the strong positive wind stress curl at the
510 typhoon's center. Furthermore, the absolute value of EPV increased in both warm eddies during the
511 typhoon's passage, but with differing impacts. The positive EPV contributed to surface water cooling and
512 the influx of cooler subsurface water, while the negative EPV facilitated downwelling and intensified the
513 influence of the warm eddies.

514 In summary, the different responses of warm eddies to typhoons provide valuable insights into the
515 complex interactions between the atmosphere and the ocean. Understanding these responses is crucial
516 for accurate climate modeling and weather forecasting. By investigating factors such as wind stress curl
517 distribution, EPV, buoyancy frequency and the relative position of the eddies to the typhoon's track,
518 researchers can gain a more precise understanding of the underlying mechanisms driving these
519 interactions. This knowledge contributes to improved predictions and mitigation strategies for the
520 impacts of typhoons and other extreme weather events, enhances the accuracy of climate models, and
521 advances weather forecasting capabilities.

522
523
524
525
526
527
528



529 *Data availability.* The six-hourly best-track typhoon datasets were accessed on 3 February 2021 by JTWC,
530 <http://www.usno.navy.mil/JTWC>, JMA, [https://www.jma.go.jp/jma/jma-eng/jma-center/rsmc-hp-pub-](https://www.jma.go.jp/jma/jma-eng/jma-center/rsmc-hp-pub-eg/besttrack.html)
531 [eg/besttrack.html](http://tcdata.typhoon.gov.cn) and CMA, <http://tcdata.typhoon.gov.cn>. The AVISO product was accessed on 14 February
532 2021 by <https://marine.copernicus.eu/>. The AVHRR SST data was accessed on 16 March, 2022 by
533 ftp://podaac.jpl.nasa.gov/documents/dataset_docs/avhrr_pathfinder_sst.html. The Argo data was accessed
534 on 4 April, 2022 by <https://dataselection.euro-argo.eu/>. The wind data was accessed on 5 January, 2023 by
535 <https://apps.ecmwf.int/datasets/data/interim-full-daily/levtype=sfc/>. The GLORYS12V1 was accessed on
536 23 March, 2022 by <https://marine.copernicus.eu/>.

537 *Author contributions.* XYL and HZ contributed to the study conception and design. Material preparation, data
538 collection and analysis were performed by YHH and XYL. GQH and YL contributed to the methodology. The
539 original manuscript was prepared by XYL and YHH. All the authors contributed to the review and editing of
540 the manuscript.

541 *Competing interests.* The contact author has declared that none of the authors has any competing interests.

542 *Disclaimer.* Publisher's note: Copernicus Publications remains neutral with regard to jurisdictional claims in
543 published maps and institutional affiliations.

544 *Acknowledgements.* These data were collected and made freely available by JTWC, JMA, CMA, AVISO, AVHRR,
545 Argo, ECMWF, COPERNICUS. All figures were created using MATLAB, in particular using the M_Map toolbox
546 (Pawlowicz, 2020). The authors thank the anonymous reviewers, whose feedback led to substantial im-
547 provement of the resulting analyses, figures and manuscript

548 *Financial support.* This research has been supported by the National Natural Science Foundation of China
549 (42227901), Southern Marine Science and Engineering Guangdong Laboratory (Zhuhai), grant number
550 SML2020SP007 and SML2021SP207; the Innovation Group Project of Southern Marine Science and
551 Engineering Guangdong Laboratory (Zhuhai), grant number 311020004 and 311022001; the National
552 Natural Science Foundation of China, grant number 42206005; the open fund of State Key Laboratory of
553 Satellite Ocean Environment Dynamics, Second Institute of Oceanography, MNR, grant number QNHX2309;
554 General scientific research project of Zhejiang Provincial Department of Education, grant number
555 Y202250609; the Open Foundation from Marine Sciences in the First-Class Subjects of Zhejiang, grant number
556 OFMS006; State Key Laboratory of Tropical Oceanography (South China Sea Institute of Oceanology Chinese
557 Academy of Sciences), grant number LTO2220.

558

559

560

561



562 **References**

- 563 Cabanes, C., Grouazel, A., von Schuckmann, K., Hamon, M., Turpin, V., Coatanoan, C., Guinehut, S.,
564 Boone, C., Ferry, N., and Reverdin, G.: The CORA dataset: validation and diagnostics of ocean
565 temperature and salinity in situ measurements, *Ocean Sci. Discuss.*, 9, 1273-1312, 2012.
- 566 Chen, G., Hou, Y., and Chu, X.: Mesoscale eddies in the South China Sea: Mean properties,
567 spatiotemporal variability, and impact on thermohaline structure, *J. Geophys. Res.: Oceans*,
568 116,<https://doi.org/10.1029/2010jc006716>, 2011.
- 569 de Boyer Montégut, C.: Mixed layer depth over the global ocean: An examination of profile data and a
570 profile-based climatology, *J. Geophys. Res.: Oceans*, 109,<https://doi.org/10.1029/2004jc002378>, 2004.
- 571 Ezraty, R., Girard-Ardhuin, F., Piollé, J.-F., Kaleschke, L., and Heygster, G.: Arctic and Antarctic sea
572 ice concentration and Arctic sea ice drift estimated from Special Sensor Microwave data, Département
573 d’Océanographie Physique et Spatiale, IFREMER, Brest, France and University of Bremen Germany, 2,
574 2007.
- 575 Han, G., Ma, Z., and Chen, N.: Hurricane Igor impacts on the stratification and phytoplankton bloom
576 over the Grand Banks, *J. Mar. Syst.*, 100-101, 19-25,<https://doi.org/10.1016/j.jmarsys.2012.03.012>, 2012.
- 577 Huang, L., Cao, R., and Zhang, S.: Distribution and Oceanic Dynamic Mechism of Precipitation Induced
578 by Typhoon Lekima, *American Journal of Climate Change*, 11, 133-
579 154,<https://doi.org/10.4236/ajcc.2022.112007>, 2022.
- 580 Huang, X. and Wang, G.: Response of a Mesoscale Dipole Eddy to the Passage of a Tropical Cyclone:
581 A Case Study Using Satellite Observations and Numerical Modeling, *Remote Sens.*,
582 14,<https://doi.org/10.3390/rs14122865>, 2022.
- 583 Jaimes, B. and Shay, L. K.: Enhanced Wind-Driven Downwelling Flow in Warm Oceanic Eddy Features
584 during the Intensification of Tropical Cyclone Isaac (2012): Observations and Theory, *J. Phys. Oceanogr.*,
585 45, 1667-1689,<https://doi.org/10.1175/jpo-d-14-0176.1>, 2015.
- 586 Jullien, S., Menkès, C. E., Marchesiello, P., Jourdain, N. C., Lengaigne, M., Koch-Larrouy, A., Lefèvre,
587 J., Vincent, E. M., and Faure, V.: Impact of tropical cyclones on the heat budget of the South Pacific
588 Ocean, *J. Phys. Oceanogr.*, 42, 1882-1906,<https://doi.org/10.1175/JPO-D-11-0133.1>, 2012.
- 589 Kessler, W. S.: The circulation of the eastern tropical Pacific: A review, *Prog. Oceanogr.*, 69, 181-
590 217,<https://doi.org/10.1016/j.pocean.2006.03.009>, 2006.
- 591 Li, Q., Sun, L., Liu, S., Xian, T., and Yan, Y.: A new mononuclear eddy identification method with
592 simple splitting strategies, *Remote Sens. Lett.*, 5, 65 - 72,<https://doi.org/10.1080/2150704x.2013.872814>,
593 2014.
- 594 Li, X., Zhang, X., Fu, D., and Liao, S.: Strengthening effect of super typhoon Rammasun (2014) on
595 upwelling and cold eddies in the South China Sea, *J. Oceanol. Limnol.*, 39, 403-
596 419,<https://doi.org/10.1007/s00343-020-9239-x>, 2021.
- 597 Lin, I. I., Chou, M.-D., and Wu, C.-C.: The Impact of a Warm Ocean Eddy on Typhoon Morakot (2009):
598 A Preliminary Study from Satellite Observations and Numerical Modelling, *TAO: Terrestrial,
599 Atmospheric and Oceanic Sciences*, 22,[https://doi.org/10.3319/tao.2011.08.19.01\(tm\)](https://doi.org/10.3319/tao.2011.08.19.01(tm)), 2011.
- 600 Lin, I. I., Wu, C.-C., Emanuel, K. A., Lee, I. H., Wu, C.-R., and Pun, I.-F.: The Interaction of
601 Supertyphoon Maemi (2003) with a Warm Ocean Eddy, *Mon. Weather Rev.*, 133, 2635-
602 2649,<https://doi.org/10.1175/MWR3005.1>, 2005.
- 603 Liu, F. and Tang, S.: Influence of the Interaction Between Typhoons and Oceanic Mesoscale Eddies on
604 Phytoplankton Blooms, *J. Geophys. Res.: Oceans*, 123, 2785-
605 2794,<https://doi.org/10.1029/2017jc013225>, 2018.



- 606 Liu, S.-S., Sun, L., Wu, Q., and Yang, Y.-J.: The responses of cyclonic and anticyclonic eddies to
607 typhoon forcing: The vertical temperature-salinity structure changes associated with the horizontal
608 convergence/divergence, *J. Geophys. Res.: Oceans*, 122, 4974-
609 4989,<https://doi.org/10.1002/2017JC012814>, 2017.
- 610 Lu, Z., Wang, G., and Shang, X.: Response of a Preexisting Cyclonic Ocean Eddy to a Typhoon, *J. Phys.*
611 *Oceanogr.*, 46, 2403-2410,<https://doi.org/10.1175/jpo-d-16-0040.1>, 2016.
- 612 Lu, Z., Wang, G., and Shang, X.: Strength and Spatial Structure of the Perturbation Induced by a Tropical
613 Cyclone to the Underlying Eddies, *J. Geophys. Res.: Oceans*, 125,<https://doi.org/10.1029/2020jc016097>,
614 2020.
- 615 Lu, Z., Wang, G., and Shang, X.: Observable large-scale impacts of tropical cyclones on subtropical gyre,
616 *J. Phys. Oceanogr.*,<https://doi.org/10.1175/JPO-D-22-0230.1>, 2023.
- 617 Ma, Z., Zhang, Z., Fei, J., and Wang, H.: Imprints of Tropical Cyclones on Structural Characteristics of
618 Mesoscale Oceanic Eddies Over the Western North Pacific, *Geophys. Res. Lett.*,
619 48,<https://doi.org/10.1029/2021gl092601>, 2021.
- 620 Ma, Z., Fei, J., Liu, L., Huang, X., and Li, Y.: An Investigation of the Influences of Mesoscale Ocean
621 Eddies on Tropical Cyclone Intensities, *Mon. Weather Rev.*, 145, 1181-
622 1201,<https://doi.org/10.1175/mwr-d-16-0253.1>, 2017.
- 623 Mei, W., Lien, C.-C., Lin, I. I., and Xie, S.-P.: Tropical Cyclone-Induced Ocean Response: A
624 Comparative Study of the South China Sea and Tropical Northwest Pacific*, *J. Clim.*, 28, 5952-
625 5968,<https://doi.org/10.1175/jcli-d-14-0065.1>, 2015.
- 626 Mitarai, S. and McWilliams, J. C.: Wave glider observations of surface winds and currents in the core of
627 Typhoon Danas, *Geophys. Res. Lett.*, 43, 11312-11319,<https://doi.org/10.1002/2016gl071115>, 2016.
- 628 Ning, J., Xu, Q., Zhang, H., Wang, T., and Fan, K.: Impact of Cyclonic Ocean Eddies on Upper Ocean
629 Thermodynamic Response to Typhoon Soudelor, *Remote Sens.*, 11,<https://doi.org/10.3390/rs11080938>,
630 2019.
- 631 Oey, L. Y., Ezer, T., Wang, D. P., Fan, S. J., and Yin, X. Q.: Loop Current warming by Hurricane Wilma,
632 *Geophys. Res. Lett.*, 33,<https://doi.org/10.1029/2006gl025873>, 2006.
- 633 Price, J. F.: Upper Ocean Response to a Hurricane, *J. Phys. Oceanogr.*,[https://doi.org/10.1175/1520-0485\(1981\)011%3C0153:UORTAH%3E2.0.CO;2](https://doi.org/10.1175/1520-0485(1981)011%3C0153:UORTAH%3E2.0.CO;2), 1981.
- 635 Pujol, M.-I., Faugère, Y., Taburet, G., Dupuy, S., Pelloquin, C., Ablain, M., and Picot, N.: DUACS
636 DT2014: the new multi-mission altimeter data set reprocessed over 20 years, *Ocean Sci.*, 12, 1067-
637 1090,<https://doi.org/10.5194/os-12-1067-2016>, 2016.
- 638 Rudzin, J. E. and Chen, S.: On the dynamics of the eradication of a warm core mesoscale eddy after the
639 passage of Hurricane Irma (2017), *Dyn. Atmos. Oceans*,
640 100,<https://doi.org/10.1016/j.dynatmoce.2022.101334>, 2022.
- 641 Shang, X.-d., Zhu, H.-b., Chen, G.-y., Xu, C., and Yang, Q.: Research on Cold Core Eddy Change and
642 Phytoplankton Bloom Induced by Typhoons: Case Studies in the South China Sea, *Adv. Meteorol.*, 2015,
643 1-19,<https://doi.org/10.1155/2015/340432>, 2015.
- 644 Shay, L. K. and Jaimes, B.: Mixed Layer Cooling in Mesoscale Oceanic Eddies during Hurricanes
645 Katrina and Rita, *Mon. Weather Rev.*, 137, 4188-4207,<https://doi.org/10.1175/2009mwr2849.1>, 2009.
- 646 Shay, L. K. and Jaimes, B.: Near-Inertial Wave Wake of Hurricanes Katrina and Rita over Mesoscale
647 Oceanic Eddies, *J. Phys. Oceanogr.*, 40, 1320-1337,<https://doi.org/10.1175/2010jpo4309.1>, 2010.



- 648 Shay, L. K., Goni, G. J., and Black, P. G.: Effects of a Warm Oceanic Feature on Hurricane Opal, Mon.
649 Weather Rev., 128, 1366-1383, [https://doi.org/10.1175/1520-0493\(2000\)128<1366:EOAWOF>2.0.CO;2](https://doi.org/10.1175/1520-0493(2000)128<1366:EOAWOF>2.0.CO;2), 2000.
- 651 Song, D., Guo, L., Duan, Z., and Xiang, L.: Impact of Major Typhoons in 2016 on Sea Surface Features
652 in the Northwestern Pacific, Water, 10, <https://doi.org/10.3390/w10101326>, 2018.
- 653 Stramma, L., Cornillon, P., and Price, J. F.: Satellite observations of sea surface cooling by hurricanes,
654 J. Geophys. Res.: Oceans, 91, 5031-5035, <https://doi.org/10.1029/JC091iC04p05031>, 1986.
- 655 Sun, J., Ju, X., Zheng, Q., Wang, G., Li, L., and Xiong, X.: Numerical Study of the Response of Typhoon
656 Hato (2017) to Grouped Mesoscale Eddies in the Northern South China Sea, J. Geophys. Res.: Atmos.,
657 128, <https://doi.org/10.1029/2022jd037266>, 2023.
- 658 Sun, L., Yang, Y., Xian, T., Lu, Z., and Fu, Y.: Strong enhancement of chlorophyll a concentration by a
659 weak typhoon, Mar. Ecol. Prog. Ser., 404, 39-50, <https://doi.org/10.3354/meps08477>, 2010.
- 660 Sun, L., Li, Y.-X., Yang, Y.-J., Wu, Q., Chen, X.-T., Li, Q.-Y., Li, Y.-B., and Xian, T.: Effects of super
661 typhoons on cyclonic ocean eddies in the western North Pacific: A satellite data-based evaluation
662 between 2000 and 2008, J. Geophys. Res.: Oceans, 119, 5585-
663 5598, <https://doi.org/10.1002/2013jc009575>, 2014.
- 664 Thompson, B. and Tkalic, P.: Mixed layer thermodynamics of the Southern South China Sea, Clim.
665 Dyn., 43, 2061-2075, <https://doi.org/10.1007/s00382-013-2030-3>, 2014.
- 666 Vincent, E. M., Lengaigne, M., Madec, G., Vialard, J., Samson, G., Jourdain, N. C., Menkes, C. E., and
667 Jullien, S.: Processes setting the characteristics of sea surface cooling induced by tropical cyclones, J.
668 Geophys. Res.: Oceans, 117, n/a-n/a, <https://doi.org/10.1029/2011JC007396>, 2012.
- 669 Wada, A. and Usui, N.: Impacts of Oceanic Preexisting Conditions on Predictions of Typhoon Hai-Tang
670 in 2005, Adv. Meteorol., 2010, 756071, <https://doi.org/10.1155/2010/756071>, 2010.
- 671 Walker, N. D., Leben, R. R., and Balasubramanian, S.: Hurricane-forced upwelling and
672 chlorophyllaenhancement within cold-core cyclones in the Gulf of Mexico, Geophys. Res. Lett., 32, n/a-
673 n/a, <https://doi.org/10.1029/2005gl023716>, 2005.
- 674 Wang, G., Su, J., Ding, Y., and Chen, D.: Tropical cyclone genesis over the south China sea, J. Mar.
675 Syst., 68, 318-326, <https://doi.org/10.1016/j.jmarsys.2006.12.002>, 2007.
- 676 Wang, G., Zhao, B., Qiao, F., and Zhao, C.: Rapid intensification of Super Typhoon Haiyan: the
677 important role of a warm-core ocean eddy, Ocean Dyn., 68, 1649-1661, <https://doi.org/10.1007/s10236-018-1217-x>, 2018.
- 679 Wu, C.-R., Chiang, T.-L., and Oey, L.-Y.: Typhoon Kai-Tak: An Ocean's Perfect Storm, J. Phys.
680 Oceanogr., 41, 221-233, <https://doi.org/10.1175/2010JPO4518.1>, 2011.
- 681 Xiu, P., Chai, F., Shi, L., Xue, H., and Chao, Y.: A census of eddy activities in the South China Sea
682 during 1993–2007, J. Geophys. Res.: Oceans, 115, <https://doi.org/10.1029/2009jc005657>, 2010.
- 683 Yan, Y., Li, L., and Wang, C.: The effects of oceanic barrier layer on the upper ocean response to tropical
684 cyclones, J. Geophys. Res.: Oceans, 122, 4829-4844, <https://doi.org/10.1002/2017jc012694>, 2017.
- 685 Yu, F., Yang, Q., Chen, G., and Li, Q.: The response of cyclonic eddies to typhoons based on satellite
686 remote sensing data for 2001–2014 from the South China Sea, Oceanologia, 61, 265-
687 275, <https://doi.org/10.1016/j.oceano.2018.11.005>, 2019.
- 688 Yu, J., Lin, S., Jiang, Y., and Wang, Y.: Modulation of Typhoon-Induced Sea Surface Cooling by
689 Preexisting Eddies in the South China Sea, Water, 13, <https://doi.org/10.3390/w13050653>, 2021.



690 Zhang, H.: Modulation of Upper Ocean Vertical Temperature Structure and Heat Content by a Fast-
691 Moving Tropical Cyclone, *J. Phys. Oceanogr.*, 53, 493-508, <https://doi.org/10.1175/jpo-d-22-0132.1>,
692 2022.
693 Zhang, H., Chen, D., Zhou, L., Liu, X., Ding, T., and Zhou, B.: Upper ocean response to typhoon
694 Kalmaegi (2014), *J. Geophys. Res.: Oceans*, 121, 6520-6535, <https://doi.org/10.1002/2016jc012064>,
695 2016.
696 Zhang, Y., Zhang, Z., Chen, D., Qiu, B., and Wang, W.: Strengthening of the Kuroshio current by
697 intensifying tropical cyclones, *Science*, 368, 988-993, <https://doi.org/10.1126/science.aax5758>, 2020.
698